4.1. INTRODUCTION

Conservation of energy and the environment are crucial challenges for the advancement of the industry in the world today. The mechanical systems are invariably damaged through friction and wear. Such systems eventually have detrimental effects on the machine parts because of the immediate contact of the rubbing surfaces leading to friction and wear. The frictional losses must be massively diminished in order to conserve energy and extend the service life of mechanical components. A lubricant is introduced between the rubbing surfaces, for the purpose. Certainly, friction and wear modifiers blended with a base lube reduce friction and wear significantly. Therefore, there is always an urge to develop antiwear/antifriction agents with more efficacy.

Two-dimensional (2D) materials, for instance, single or multilayered graphene, phosphorene, hexagonal boron nitride (h-BN), layered double hydroxide (LDH), and transition metal dichalcogenides (TMDs), have been acknowledged for myriad applications, like hydrogen evolution, field effect transistors, supercapacitors, phototransistors, water desalination, lithium-ion batteries, and catalysis, etc.[1] Weak van der Waals interactions hold together the interlayers of these 2D-materials; therefore, it is possible to disperse them in an appropriate medium.[1] The existence of these forces is instrumental in enhancing the slippage of sheets over one another, thus, facilitating lubrication.[1,2] Such materials, therefore, serve as suitable lubricant additives, too. Adequate research papers and reviews are available in the literature regarding tribological studies on transition metal disulfides, mainly MoS_2 and WS_2.[2-10] Few researchers have focused on the tribological properties of the transition-metal diselenides, which had a

structure like MoS_2 and WS_2. Among these transition metal diselenides, $NbSe_2$ possesses a layered hexagonal structure, which holds outstanding self-lubricating behavior.[11] Li et al. tested the tribological performance of $NbSe_2$ fibers.[12] Yang and co-workers in HVI500 base oil investigated the lubricious behavior of WSe_2 nanorods.[13] Cao and associates synthesized ultrathin nanosheets of WSe_2 having a tower-like structure and examined their tribological behavior as a paraffin oil additive.[14] For the furtherance of the tribological performance, doping the transition-metal dichalcogenides with cations and anions has been preferred. Accordingly, nano lamellar Mo-doped WSe_2 and Nb-doped $MoSe_2$ nanoplates have been synthesized, and their tribological properties were evaluated as additives to the base oil.[15,16] Tang et al. investigated the tribological behavior of the $Cu/NbSe_2$ composite and noted its low electrical resistivity.[17]

Bismuth chalcogenides of the general formula Bi_2X_3 (where X = S, Se, Te) also possess lamellar structure and are known as the best thermoelectric materials.[18] The tribological performance of formulations of bismuth (III) sulfide in vinyl-terminated silicone fluid (PDMS-Vi) has been studied using Reichert's test (steel/steel system) and block-on ring tests (polymer/steel).[19] Formation of bismuth sulfide has been reported during testing of bismuth carboxylate-polysulfide mixtures as the extreme pressure additives.[20] The behavior of bismuth sulfide as a powder lubricant was studied at temperatures up to 580 °C.[21] The frictional behavior of burnished Bi_2S_3 soft coatings was evaluated utilizing reciprocating sliding tests.[22]

On the other hand, Bi_2Se_3 retains a rhombohedral crystal structure of the space group D_{3d} (R3m).[18] The quintuple layers of Bi_2Se_3 containing Se-Bi-Se-Bi-Se atoms bonded

covalently are fastened together by weak van der Waals forces.[18,23] To the best of our knowledge, selenide of bismuth (Bi_2Se_3) has never been used as a lubricant additive. Thus like Bi_2S_3, Bi_2Se_3 is anticipated to be a promising lubricant additive.

Oxysalts like chromates, sulfates, tungstates, molybdates, and vanadates have been highlighted in the literature for their exemplary lubricity owing to low shear strength and high ductility at high temperatures.[24-29] Numerous tungstates like $CuWO_4$, $ZnWO_4$, $CaWO_4$, and $PbWO_4$ have been proven as solid lubricants.[24,30] Bismuth tungstate (Bi_2WO_6), a non-toxic n-type semiconductor (bandgap 2.8 eV) with high chemical and thermal stability, possesses an orthorhombic crystal structure.[31,32] It is an Aurivillius-phase perovskite containing alternating fluorine-like layers $[Bi_2O_2]^{2+}$ and perovskite layers $[WO_4]^{2-}$. [31,33] So like other tungstates, bismuth tungstate (Bi_2WO_6) was synthesized to explore its lubricious behavior, which has not been used in tribology. It has been reported that doped nanomaterials, due to the creation of defects, lead to the formation of slip systems that can change the electronic structure and lower the shear strength; ultimately, tribological properties are enhanced.[2,3,34-36] Nitrogen-doped Bi_2WO_6 was therefore synthesized for the advancement of lubrication performance.

Hou and Leven et al. presented that heterostructures made by piling two different types of 2D nanomaterials, for instance, graphene/MoS_2 and graphene/h-BN, exhibit an almost double decrement in interlayer shear strength relative to homogeneous bilayers.[37,38] Accordingly, tribological characteristics of heterostructures are significantly improved as compared to homogeneous ones. Likewise, coupling 2D g-C_3N_4 nanosheets with MoS_2 nanosheets resulted in outstanding tribological behavior.[39] Motivated by the above

observations, it was speculated that the Bi_2Se_3/Bi_2WO_6 and Bi_2Se_3/N-Bi_2WO_6 hybrids might be effective additives to improve the tribological behavior of base oil. Consequently, the nanosheets of Bi_2Se_3, Bi_2WO_6, N-Bi_2WO_6, and the hybrids Bi_2Se_3/Bi_2WO_6, Bi_2Se_3/N-Bi_2WO_6 were prepared, and their tribological activity was evaluated using a four-ball lubricant tester following ASTM D4172 and D5183 guidelines.

4.2. EXPERIMENTAL METHODS

4.2.1. Materials

Analytical Reagent grade chemicals utilized throughout the work were purchased from Merck India.

4.2.2. Preparation of Nano-Additives

4.2.2.1. Preparation of lamellar Bi_2Se_3 nanosheets

For the preparation of Bi_2Se_3, bismuth nitrate pentahydrate $Bi(NO_3)_3{\cdot}5H_2O$ was used as the Bi^{3+} source, and powdered selenium with reductant $NaBH_4$ as the Se^{2-} source.[23] At first $Bi(NO_3)_3{\cdot}5H_2O$ (0.293 g) was dispersed in ethanol (55 ml) by stirring the solution for 30 min. Selenium powder (0.071 g) and $NaBH_4$ (0.068 g) were mixed in ethanol (15 ml) with continuous stirring until a transparent and clear solution was obtained. The prepared mixture of $Bi(NO_3)_3{\cdot}5H_2O$ and sodium selenide obtained by 1 h stirring was transferred into a Teflon-lined autoclave (capacity 100 ml) and kept inside an oven for 24 h at 180 °C. Subsequently, the resultant product of the autoclave was cooled down naturally to ambient temperature. The black-colored Bi_2Se_3 powder was filtered and then Repeatedly washed with distilled water and ethanol and dried at 60 °C in a vacuum oven

for 10 h. For exfoliation, the obtained black powder was taken in the ethanol-water mixture (1:1) and ultrasonicated for 4 h to yield Bi_2Se_3 nanosheets.

4.2.2.2. Preparation of bismuth tungstate nanosheets (Bi_2WO_6)

Initially, sodium tungstate ($Na_2WO_4.2H_2O$) (1 mmol), $Bi(NO_3)_3.5H_2O$ (2 mmol), cetyltrimethylammonium bromide (CTAB) (0.05 g), and 80 mL distilled water were intermixed by stirring continuously for 30 min. The obtained mixture was poured into a sealed Teflon-lined stainless-steel autoclave and heated in an oven for 24 h at 140 °C. After cooling to room temperature, the product was removed via centrifugation and washed thoroughly with water and ethanol separately. Lastly, it was dried in an oven for 10 h at 60 °C and exfoliated by ultrasonication for 4 h in the ethanol-water mixture (1:1) to obtain the Bi_2WO_6 nanosheets.[31]

4.2.2.3. Preparation of N-Bi_2WO_6 nanosheets

In order to prepare N-Bi_2WO_6 nanosheets, a hydrothermal approach was applied.[40] Firstly, $Na_2WO_4.2H_2O$ (1 mmol) and $Bi(NO_3)_3.5H_2O$ (2 mmol) were mixed in distilled water by stirring at room temperature for 1 h. For nitrogen doping, an aqueous solution of urea (2 mmol) was added as a nitrogen source to the above mixture (N to Bi atomic ratio was taken as 2.0) and transferred into a Teflon-lined autoclave and kept in an oven for 24 h at 160 °C. When the autoclave naturally cooled to ambient temperature, the obtained suspension was filtered and washed with distilled water and ethanol several times to ensure that no anions remained in the solution. Finally, the bulk product was collected by drying up to 80 °C for 8-10 hours and exfoliated (as mentioned above) to yield the N-Bi_2WO_6 nanosheets.

4.2.2.4. Preparation of Bi_2Se_3/Bi_2WO_6 hybrid nanosheets

The dispersions of Bi_2Se_3 nanosheets (200 mg) and Bi_2WO_6 nanosheets (300 mg) were made in ethanol (50 mL) separately by ultrasonication for 30 min at about 50 ^oC. The resulting dispersions were mingled and refluxed for 24 h at 80 °C with continuous stirring. After achieving room temperature, the reaction mixture was filtered and dried at 60 °C. Lastly, a greyish-black nanohybrid containing heterostructure (Bi_2Se_3/Bi_2WO_6) was obtained.

4.2.2.5. Preparation of Bi_2Se_3/N-Bi_2WO_6 hybrid nanosheets

The Bi_2Se_3 nanosheets (200 mg) and N-Bi_2WO_6 nanosheets (300 mg) were dispersed in ethanol (100 ml). The dispersion was refluxed at 80 °C for 24 h. The hybrid Bi_2Se_3/N-Bi_2WO_6 was obtained following the same procedure as that for the Bi_2Se_3/Bi_2WO_6 hybrid. The schematic illustration for synthesizing composite Bi_2Se_3/N-Bi_2WO_6 is presented in Scheme 4.1.

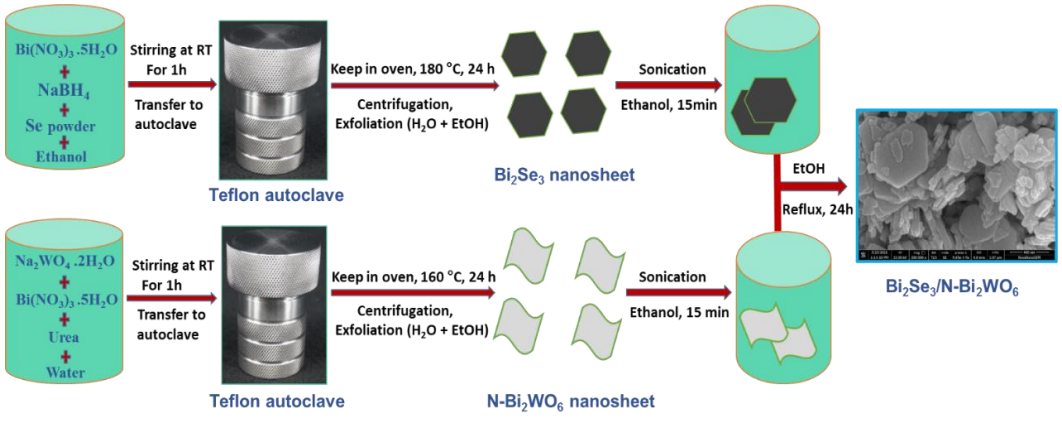

Scheme 4.1. Schematic presentation for the preparation of Bi_2Se_3/N-Bi_2WO_6

4.2.3. Sample preparation

Test samples of different concentrations in the PO, 0.000, 0.025, 0.050, 0.075, and 0.100

% w/v were prepared via 1 h sonication at room temperature. The tribological tests were performed at an optimized concentration, i.e., 0.05% w/v in base oil.

4.3. RESULTS AND DISCUSSION

4.3.1. Microstructure and Morphology of the Synthesized Additives

For the characterization of the synthesized lubricant additives, namely Bi_2Se_3, Bi_2WO_6, N-Bi_2WO_6, Bi_2Se_3/Bi_2WO_6, and Bi_2Se_3/N-Bi_2WO_6, the techniques such as XRD, FTIR, UV/visible, SEM/HR-SEM and TEM/HR-TEM have been put to practice. Also, XPS has been utilized to characterize Bi_2Se_3/N-Bi_2WO_6. XRD patterns of the as-synthesized additives Bi_2Se_3, Bi_2WO_6, N-Bi_2WO_6, Bi_2Se_3/Bi_2WO_6, and Bi_2Se_3/N-Bi_2WO_6 are presented in Figure 4.1a. As indicated by Figure 4.1a, the diffraction peaks of Bi_2Se_3 could be firmly indexed to the rhombohedral crystal geometry (JCPDS: 33-0214).[41] The planes (015), (10$\underline{1}$0), (10$\underline{1}$5), (205), (02$\underline{1}$0), and (11$\underline{1}$5) could be clearly indexed to the six main peaks of the Bi_2Se_3 rhombohedral lattice phase.[42,43] Moreover, the presence of sharp peaks indicates the highly crystalline nature of these nanosheets.[41] In the binary composites, Bi_2Se_3/Bi_2WO_6 and Bi_2Se_3/N-Bi_2WO_6, the rhombohedral lattice phase structure of Bi_2Se_3 is retained. In the diffraction pattern of Bi_2WO_6, the peaks at 2θ values of 28.4°, 32.8°, 47.1°, 55.8°, and 58.6° could be indexed to (1 1 3), (0 0 6)/(2 0 0)/(0 2 0), (0 2 6)/(2 0 6)/(2 2 0), (1 1 9)/(2 0 8)/(3 1 3) and (2 2 6) crystal planes respectively for orthorhombic structure (JCPDS No. 73-2020).[31] These peaks move slightly toward the lower angle in the case of Bi_2Se_3/Bi_2WO_6.[39] For N-Bi_2WO_6, the XRD pattern corresponds well to the pure Bi_2WO_6 phase (JCPDS No. 39-0256).[40] However, the characteristic peak of the N-Bi_2WO_6 at 2θ, 28.3 (hkl) plane (131) is slightly shifted as compared to pristine

Bi_2WO_6, which may be attributed to the substitution of the O^{2-} (0.140 nm) by the N^{3-} (0.171 nm) confirming the successful doping of nitrogen in Bi_2WO_6.[40] A slight shift in the peaks towards a lower angle was also detected in the diffraction pattern of the hybrid Bi_2Se_3/N-Bi_2WO_6, possibly due to the significant interaction between both types of nanosheets.

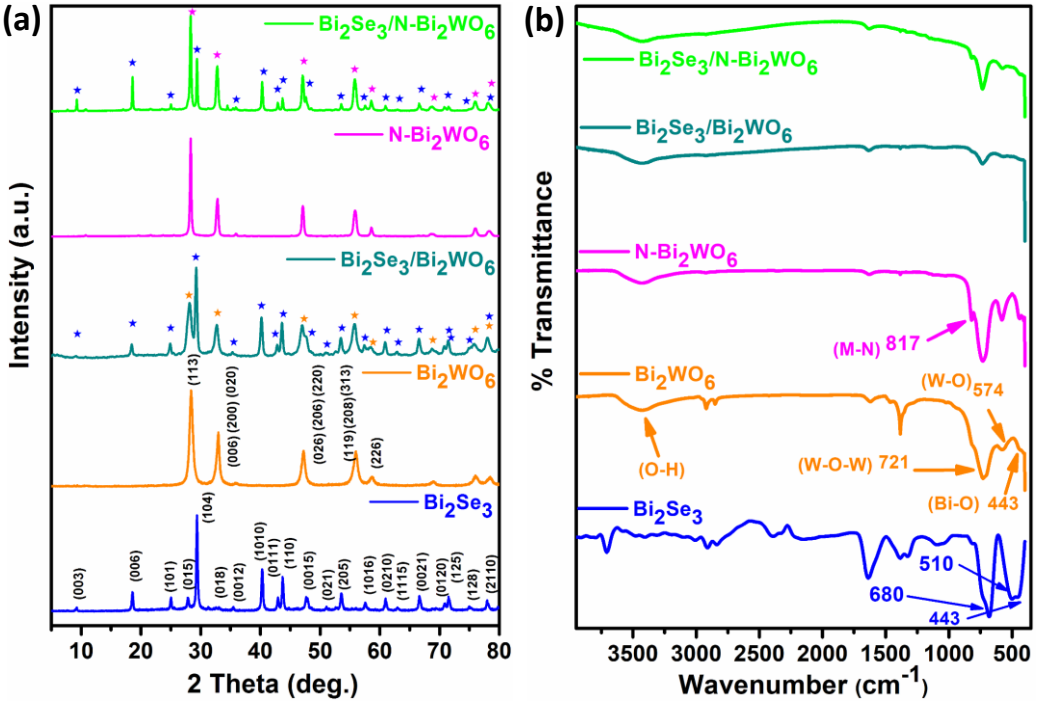

Figure 4.1. (a) XRD patterns and (b) IR spectra of Bi_2Se_3, Bi_2WO_6, N-Bi_2WO_6, Bi_2Se_3/Bi_2WO_6, and Bi_2Se_3/N-Bi_2WO_6

Figure 4.1b exhibits the IR spectra of the nano additives. The three bands observable at ~ 443, ~ 510, and ~ 680 cm^{-1} in the FTIR spectrum of Bi_2Se_3, are characteristic of Bi–Se stretching vibrations.[44] These bands are found at an identical position in the hybrid Bi_2Se_3/Bi_2WO_6 and Bi_2Se_3/N-Bi_2WO_6. The spectrum of Bi_2WO_6 exhibits prominent absorption bands in the range of 400-800 cm^{-1}, ascribed to stretching modes of Bi–O, W–

O, and bridging W–O–W.[45] These bands remain unaffected in Bi_2Se_3/Bi_2WO_6, demonstrating that no change in the structure of Bi_2WO_6 has occurred during the hybrid formation. The spectrum of N-Bi_2WO_6 exhibits an extra peak at 817 cm^{-1}, which corresponds to the vibration mode of the metal-nitrogen (W/Bi–N) bond.[46] The distinctive peaks of Bi_2Se_3 and N-Bi_2WO_6 are visible in the spectrum of the nanohybrid Bi_2Se_3/ N-Bi_2WO_6.

HR-SEM images of the Bi_2Se_3, Bi_2WO_6, N-Bi_2WO_6, Bi_2Se_3/Bi_2WO_6, and Bi_2Se_3/N-Bi_2WO_6 have been examined to study microstructural and morphological features, Figure 4.2a-e. 2D hexagonal layered morphology is evident for Bi_2Se_3,[41] Figure 4.2a, with an average lateral size of 400-800 nm and thicknesses of 30-70 nm. As shown in Figure 4.2b, Bi_2WO_6 exhibits randomly stacked layered morphology with an average lateral size of 50-400 nm and a 10-15 nm thickness. The nanosheets of N-Bi_2WO_6 shown in Figure 4.2c indicate a thickness of about 20-40 nm and lateral size in the range of 150-450 nm. It is noticed evidently in Figure 4.2d that the nano-sheets of Bi_2WO_6 are self-assembled on the surface of Bi_2Se_3 layers to fabricate a 2D/2D hybrid structure. As compared to pure Bi_2WO_6, the allocation of Bi_2WO_6 nanosheets on the surface of Bi_2Se_3 is even and separated from each other in the composite. Figure 4.2e exhibits the coexistence of separated nanosheets of N-Bi_2WO_6 adorning Bi_2Se_3 nanosheets. Figure 4.2f divulges the EDX spectrum of the binary nanohybrid Bi_2Se_3/N-Bi_2WO_6. The advent of perceivable peaks for the elements bismuth, selenium, and tungsten, besides nitrogen and oxygen, corroborate the existence of Bi_2Se_3/N-Bi_2WO_6. EDX spectra of Bi_2Se_3, Bi_2WO_6, N-Bi_2WO_6, and Bi_2Se_3/Bi_2WO_6 have been provided in Figure 4.3.

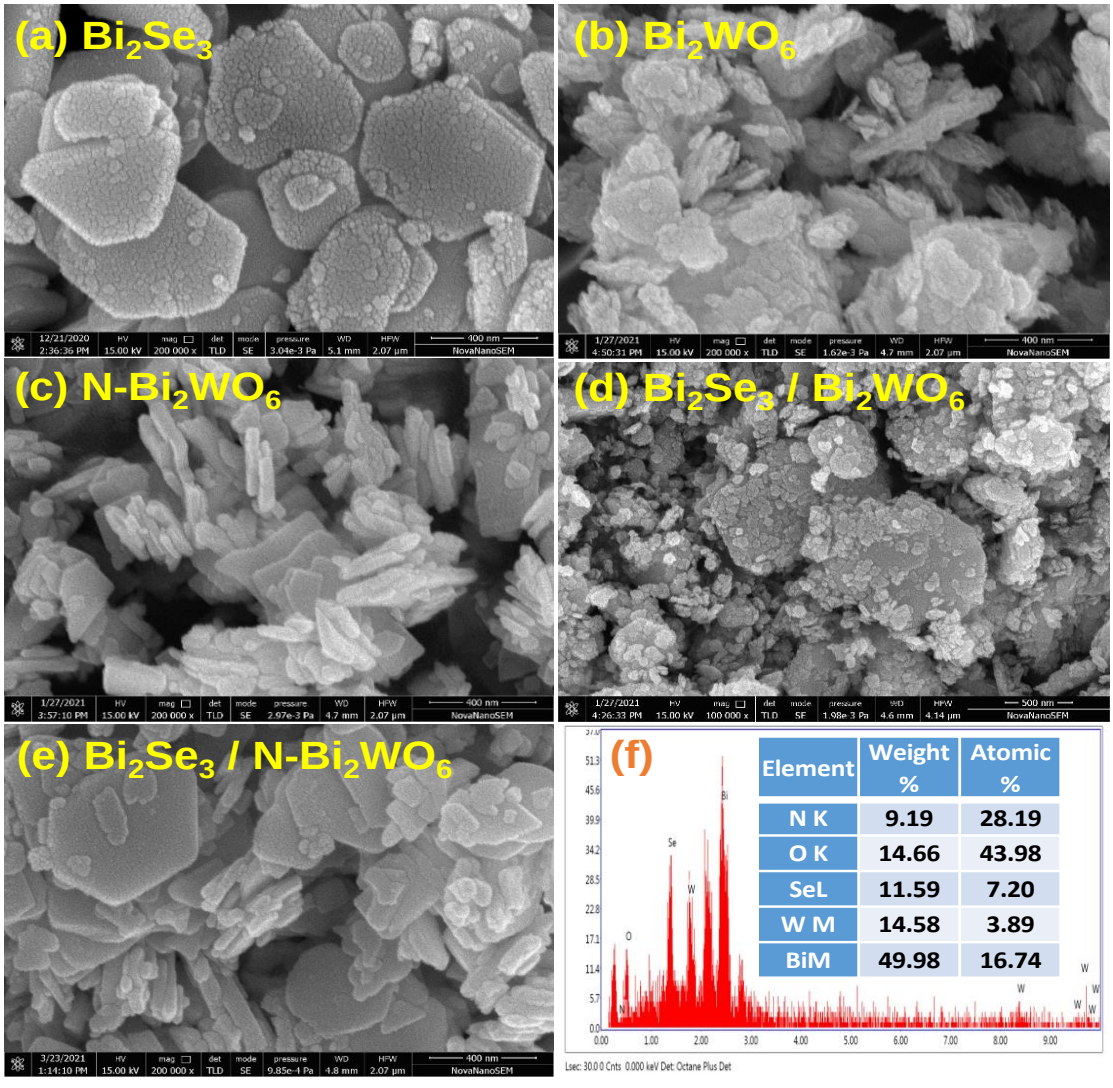

Figure 4.2. HR-SEM images of (a) Bi_2Se_3, (b) Bi_2WO_6, (c) N-Bi_2WO_6, (d) Bi_2Se_3/Bi_2WO_6, (e) Bi_2Se_3/N-Bi_2WO_6 and (f) EDX spectrum of Bi_2Se_3/N-Bi_2WO_6

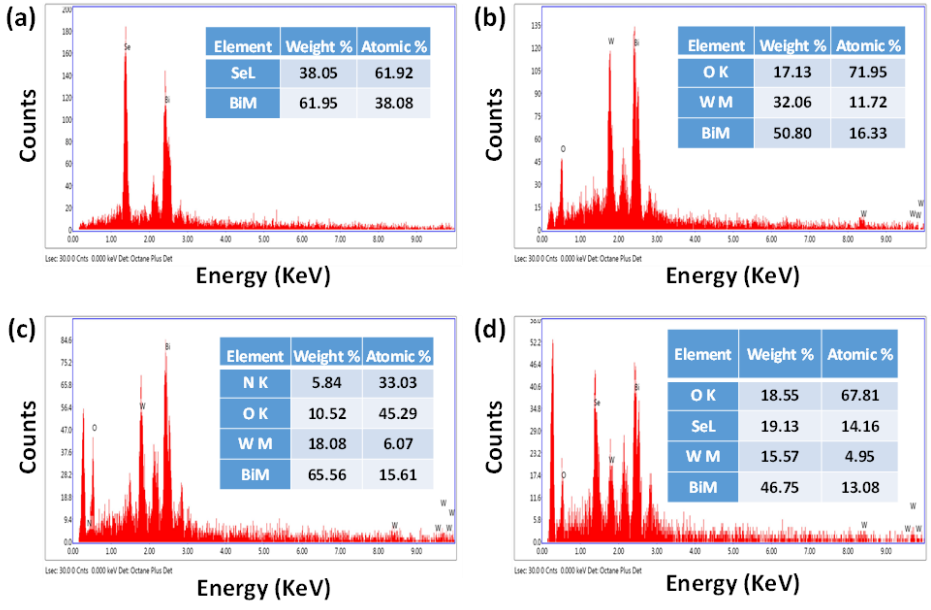

Figure 4.3. EDX spectrum of, (a) Bi_2Se_3, (b) Bi_2WO_6, (c) N-Bi_2WO_6 and (d) Bi_2Se_3/Bi_2WO_6

TEM images of prepared additives have also been taken to understand refined morphology better, and are depicted in Figure 4.4a-e, respectively. The TEM image of Bi_2Se_3 nanosheets is illustrated in Figure 4.4a, indicating hexagonal geometry. Its HR TEM picture (Figure 4.4a_1) exhibits the interplanar spacing between the lattice fringes as 0.31 nm for the plane (015).[42] A lamellar morphology of Bi_2WO_6 comprising square nanosheets of about 60 nm edge lengths is clearly visible in Figure 4.4b. The interplanar separation was measured to be 0.271 and 0.272 nm, corresponding to crystallographic planes (020) and (200), respectively, for orthorhombic Bi_2WO_6 crystal.[31] Figure 4.4c divulges a well-defined nanosheet structure for N-Bi_2WO_6. The lattice fringes of the nanosheets were measured to be 0.26 nm matching the (020) plane. The anchored nanosheets of Bi_2WO_6 and N-Bi_2WO_6 on Bi_2Se_3 nanosheets in the hybrids

Bi_2Se_3/Bi_2WO_6 and Bi_2Se_3/N-Bi_2WO_6, respectively, are depicted in corresponding Figure 4.4d and 4.4e. HR-TEM images of the hybrids, Bi_2Se_3/Bi_2WO_6 and Bi_2Se_3/N-Bi_2WO_6, reveal the interlayer distance of the Bi_2Se_3 associated with the (015) plane has risen from 0.31 nm to 0.34 nm (Figures 4.4d_1 and 4.4e_1). The increase in interlayer distance of the (015) plane in Bi_2Se_3 indicates that Bi_2Se_3 nanosheets have interacted efficiently with Bi_2WO_6 and N-Bi_2WO_6 in their respective composites.[2,34,35] The selected-area electron diffraction (SAED) patterns of the as-synthesized additives, in the inset of corresponding Figures, demonstrate their polycrystalline nature.

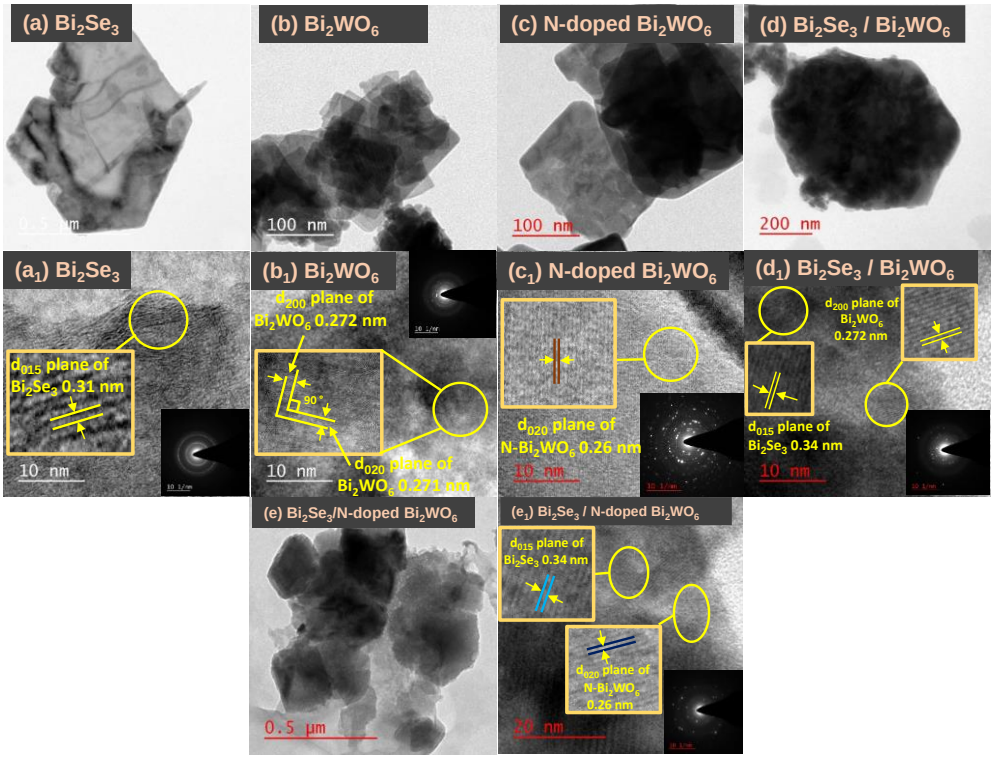

Figure 4.4. TEM snapshots of (a) Bi_2Se_3, (b) Bi_2WO_6, (c) N-Bi_2WO_6, (d) Bi_2Se_3/Bi_2WO_6 (e) Bi_2Se_3/N-Bi_2WO_6 and HR-TEM photographs of Bi_2Se_3(a_1), Bi_2WO_6(b_1), N-Bi_2WO_6(c_1), Bi_2Se_3/Bi_2WO_6(d_1), and Bi_2Se_3/N-Bi_2WO_6(e_1). SAED patterns of the additives in the insets of Figures a_1, b_1, c_1, d_1, and e_1

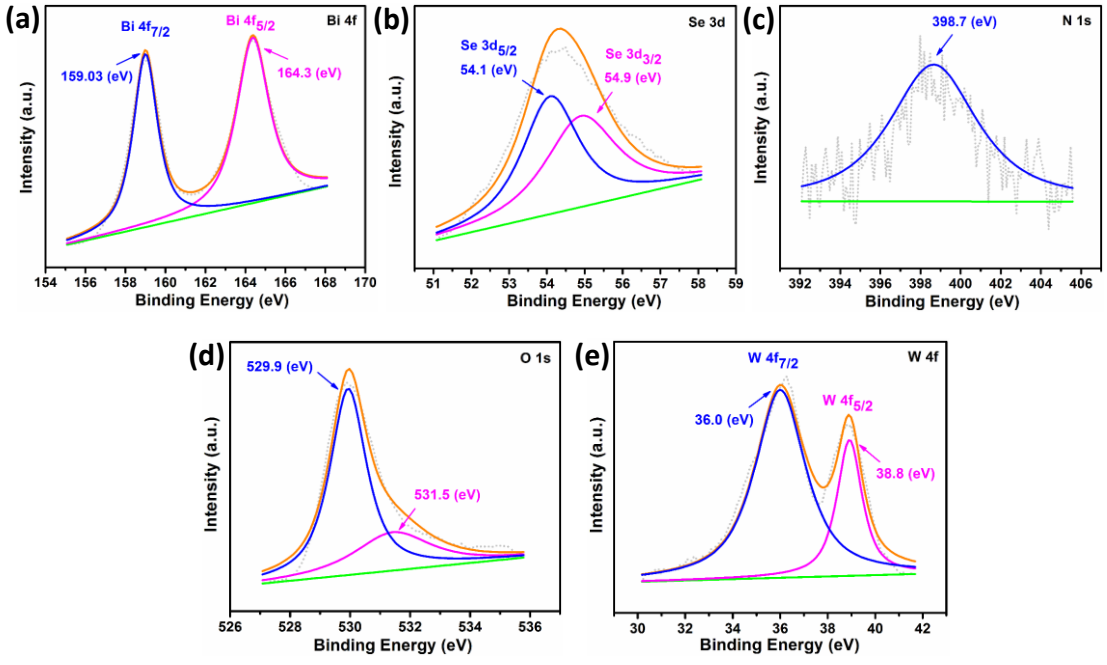

Figure 4.5. Deconvoluted core-level XPS spectra of Bi_2Se_3/N-Bi_2WO_6 nanocomposite: (a) Bi 4f, (b) Se 3d, (c) N 1s, (d) O 1s, and (e) W 4f

XPS was utilized to identify the chemical states of the elemental components in the composite Bi_2Se_3/N-Bi_2WO_6. Figure 4.5 reflects the deconvoluted core level spectra of Bi 4f, Se 3d, N 1s, O 1s, and W 4f employing the peak fitting software. The high-resolution XP spectrum of Bi 4f has been shown in Figure 4.5a exhibiting the peak position at binding energies around 159.03 eV and 164.3 eV, corresponding to the Bi $4f_{7/2}$ and Bi $4f_{5/2}$, respectively, attributed to the presence of Bi^{3+} ion for both Bi_2Se_3 and Bi_2WO_6.[31,47,48] In the XP spectra of Se 3d, two characteristic peaks depicted (Figure 4.5b) at binding energies 54.1 eV and 54.9 eV are ascribed to Se $3d_{5/2}$ and $3d_{3/2}$, corresponding to the Se^{2-}. [47] The peak position at 398.7 eV in the N 1s XP spectra (Figure 4.5c) is assigned for metal-nitrogen (W/Bi-N) bond formation in place of the metal-oxygen (W/Bi-O) bond in the lattice.[49] Figure 4.5d exhibits two peaks in the O 1s spectrum at

binding energy 529.9 and 531.5 eV, corresponding to the M-O bond (W/Bi-O) and adsorbed water molecule.[48] In the W 4f XP spectra, peaks positioned at 36.0 and 38.8 eV represent W $4f_{7/2}$ and W $4f_{5/2}$, respectively, indicating the existence of W^{6+} ion (Figure 4.5e).[48]

4.3.2. Tribological characteristics of the additives

4.3.2.1. Determination of Stability of Nanofluids

The endurance of the dispersion stability of the nano additives is essentially desiderated in addition to significant tribological performance. The dispersion stability of additives in PO at the optimized concentration (ten times diluted) has been achieved with the help of UV/visible spectroscopy (Figure 4.6a). The absorbance values of the admixtures were measured within the limits of 200-800 nm wavelength starting from zero to 72 h at a certain interval. The variation of relative absorbance with settling time is portrayed in Figure 4.6a. Although the decrement in the relative absorbance with time is observed for all the admixtures, it is minimum assuredly for the doped hybrid material Bi_2Se_3/N-Bi_2WO_6 followed by Bi_2Se_3/Bi_2WO_6 then N-Bi_2WO_6, Bi_2WO_6, and, at last maximum for Bi_2Se_3. Undoubtedly, the highest stability is apparent for the most effective additive Bi_2Se_3/N-Bi_2WO_6, but the remaining additives also possessed sufficient stability. The Figure inset shows the absorbance of Bi_2Se_3/N-Bi_2WO_6 at around 244 nm from zero to 72 h. The photographs of PO and its dispersions with different nano additives captured from the first day to the third day have been provided in Figure 4.6b

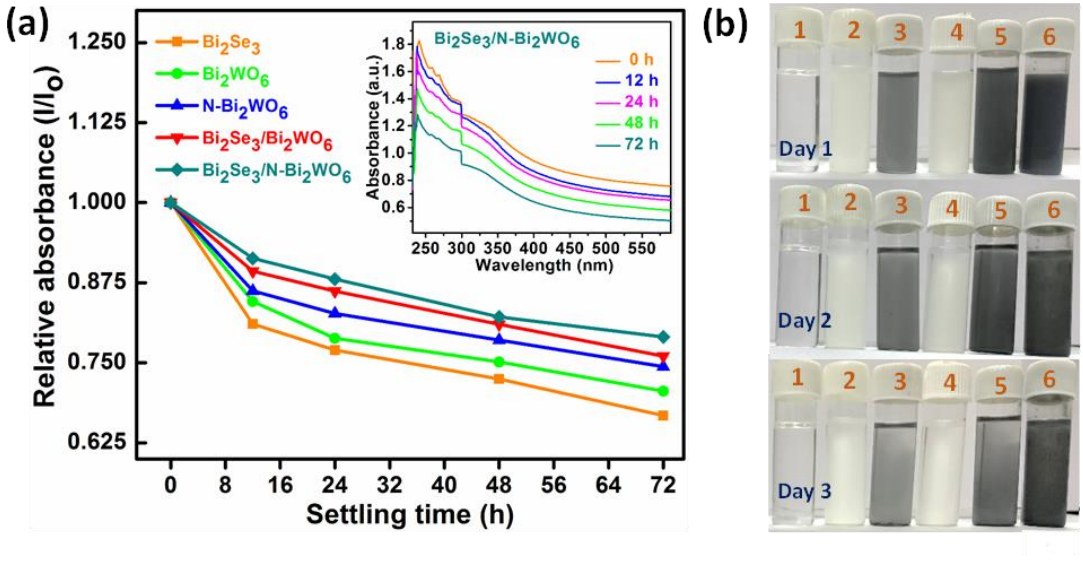

Figure 4.6. (a) Dispersion stabilities of base lube containing Bi_2Se_3, Bi_2WO_6, N-Bi_2WO_6, Bi_2Se_3/Bi_2WO_6, and Bi_2Se_3/N-Bi_2WO_6 using UV-vis spectrophotometry, (b) Photographs of the admixtures from the day 1-3

4.3.2.2. Assessment of Optimal Additive Concentration

Concerning additives' effectiveness, the most crucial variable is concentration, so it needs to be optimized first. For optimization, standard test ASTM D4172 (at 1200 rpm, 392 N applied load, time 1 h) has been conducted for blends of additives of various concentrations; 0.000, 0.025, 0.050, 0.075, and 0.100% w/v, in paraffin oil and their respective mean wear scar diameter (MWD) are reported in Figure 4.7a. Compared with the base lube, a significant reduction in MWD values is noted for every examined concentration of all the additives. Accordingly, at every tested concentration, all the examined additives serve as antiwear additives, although efficiencies are found to be vastly different. The MWD for plain PO has been marked as 0.735 mm. The relative antiwear activity of all the additives is superior to plain oil. The value of MWD decreases

from plain lube to higher concentrations, 0.025 and 0.050 % w/v; however, it increases further in general for the next concentrations except in the case of Bi_2WO_6 and N-Bi_2WO_6, where MWD increases after 0.075% w/v. Consequently, the concentration of 0.050% of w/v has been regarded as the optimized concentration for conducting tribological tests.

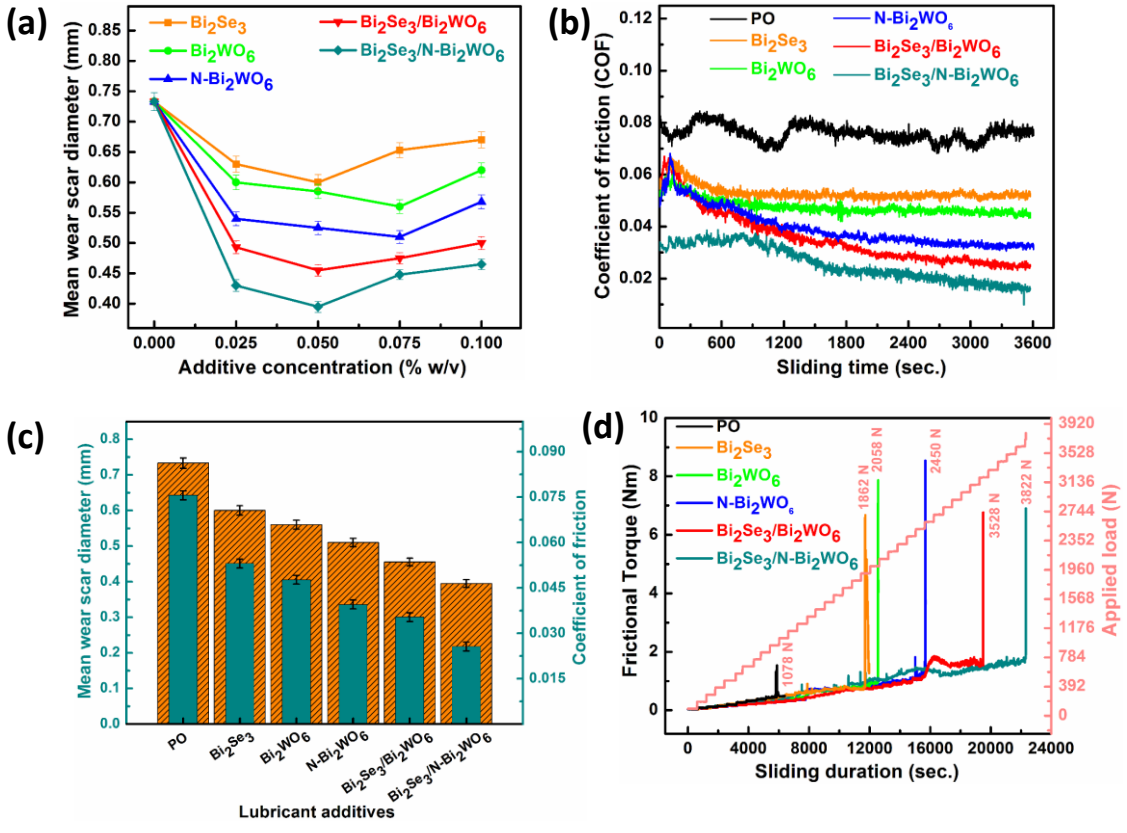

Figure 4.7. (a) Variation of MWD against the concentrations of various additives (b) COF against sliding time (c) average coefficient of friction and the MWD in the format of bar diagram (d) frictional torque *vs.* load and time for plain PO and with different additives under ASTM D5183 standards

The MWD decreases in the order of Bi_2Se_3 (0.600 mm), Bi_2WO_6 (0.570 mm), N-Bi_2WO_6 (0.530 mm), Bi_2Se_3/Bi_2WO_6 (0.470 mm), and Bi_2Se_3/N-Bi_2WO_6 (0.430 mm). Thus,

doped binary nanohybrid Bi_2Se_3/N-Bi_2WO_6 exhibits the maximum reduction in MWD among all the tested additives and has been considered the best performer with improved tribological activity.

The change in COF with time for plain paraffin oil and blends of additives was demonstrated in Figure 4.7b. Initially, the value of COF is considerably high for the base lube and its additives blends due to the lack of tribofilm formation. The COF drops down with the initiation of in situ tribofilm formation and becomes stable when tribofilm is accomplished. The outstanding friction and wear modifier efficiency of nano additives can be validated by the smoothness of the COF graph, which is irregular in the case of PO. The smoothness of the graph corresponds to the nature of the tribofilm.[35] In the case of doped binary nanohybrid, Bi_2Se_3 and N-Bi_2WO_6 nanosheets have, therefore, substantially interacted to form an adherent, uniform, and stable tribofilm, separating the mating surfaces efficiently to give significant MWD and COF values.

4.3.2.3. Antiwear and Antifriction Properties

The standard test ASTM D4172 was executed for blends of all the additives in PO to explore their antiwear activity. The observed crucially important parameters MWD and COF are displayed concurrently in the form of a bar diagram, Figure 4.7c. From the graph, it is evident that MWD regularly decreases from plain PO (0.735mm) to all the admixtures. The % reduction lies in the order; Bi_2Se_3 (18.36%), Bi_2WO_6 (22.44%), N-Bi_2WO_6 (27.89%), Bi_2Se_3/Bi_2WO_6 (36.05%), and lastly Bi_2Se_3/N-Bi_2WO_6 (41.49%). The decrement in MWD is a suggestive measure of antiwear efficiency.

Comparing the average COF for the different admixtures, analogous progression is obser

-ved in % reduction in tune with MWD. Therefore, a considerable decrease in COF of PO (0.0756) was found in the presence of the additives; Bi_2Se_3 (29.76%), Bi_2WO_6 (36.90%), N-Bi_2WO_6 (47.75%), Bi_2Se_3/Bi_2WO_6 (53.30%) and Bi_2Se_3/N-Bi_2WO_6 (66.13%) follows the similar trend as that of MWD.

4.3.2.4. Load-carrying ability

For determining the load carrying efficiency, initially, the load ramp test as per ASTM D5183 measures was conducted under the given conditions; a load of 392 N, 75 °C temperature, 600 rpm, and 1 h duration to accomplish the running-in period at the optimized concentration of the additives. Subsequently, the steady-state test was kept on by consecutive accession of 98 N load every 10 min unless a swift rise of frictional torque resulted in load seizure, as depicted in Figure 4.7d. As it is clear from the plots of frictional torque versus time and load, at 1078 N load, an abrupt increase in frictional torque appears in the case of PO, which causes the contiguous surfaces to be seized, and this load is assigned as the seizure load. At the seizure load, the tribofilm is ceased physically, and the lubricant cannot handle the load further. In the presence of additives, the failure of tribofilm occurs at relatively higher loads, and the difference in frictional torque values between base oil and the blended additives with increasing time and load has increased.[34] As shown in the Figure, the obtained seizure load (SL) for blends of additives; Bi_2Se_3 (1862 N), Bi_2WO_6 (2058 N), N-Bi_2WO_6 (2450 N), Bi_2Se_3/Bi_2WO_6 (3528 N) and Bi_2Se_3/N-Bi_2WO_6 (3822 N) manifests the load carrying capacity of the investigated additives. Accordingly, the excellent load-carrying ability is documented for the doped binary hybrid, similar to its antifriction and antiwear attributes.

Figure 4.8 illustrates the optimization of COF against additive concentration for individual additives, demonstrating that the lowest antifriction activity was observed for Bi_2Se_3, Bi_2Se_3/Bi_2WO_6, Bi_2Se_3/N-Bi_2WO_6 at a concentration of 0.050% w/v, and for Bi_2WO_6, N-Bi_2WO_6 at 0.075% w/v.

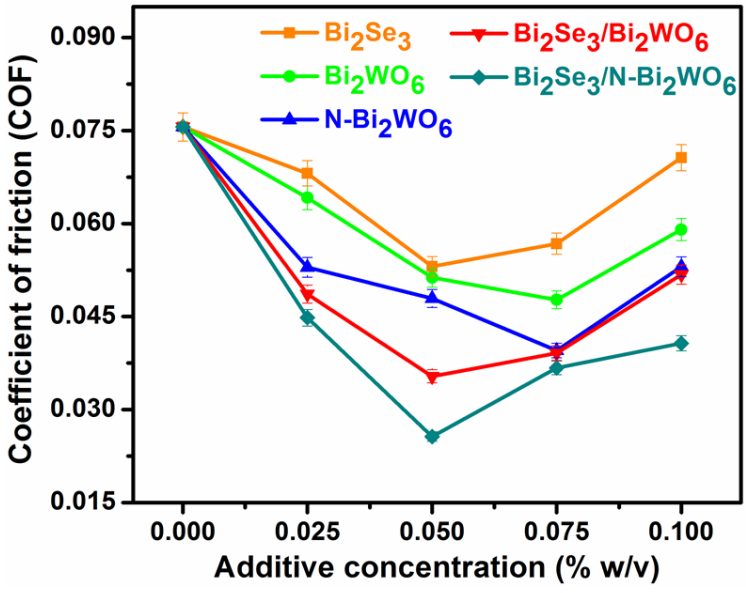

Figure 4.8. Variation of coefficient of friction (COF) vs. additive concentration

4.3.2.5. Frictional Power Loss

The calculation of values for frictional power loss (P) of base lube in the absence and presence of additive have been done by equation (4.1).

$$P = 0.221 \times 3.6 \times \mu \text{ MJ} \quad (4.1)$$

Where μ = coefficient of friction

As per the reported contents of Table 4.1, the highest power consumption of 0.0601 MJ was observed for plain oil, but for its blends with various additives, a noteworthy reduction in power consumption was perceived; 0.0422 MJ for Bi_2Se_3, 0.0379 MJ for

Bi_2WO_6, 0.0314 MJ for N-Bi_2WO_6, 0.0281 MJ for Bi_2Se_3/Bi_2WO_6 and 0.0204 MJ for the doped hybrid Bi_2Se_3/N-Bi_2WO_6. Therefore, the minimum power consumption in the case of the doped hybrid Bi_2Se_3/N-Bi_2WO_6 corresponds to maximum energy saving.

Table 4.1. Cutbacks in frictional power for individual additives in paraffin oil at the optimized concentration, 0.050 % (w/v)

S. No.	Additives	Power consumption (MJ)	Reduction in Power consumption	% Reduction in Power consumption
1.	PO	0.0601	____	____
2.	Bi_2Se_3	0.0422	0.0179	29.78
3.	Bi_2WO_6	0.0379	0.0222	36.93
4.	N-Bi_2WO_6	0.0314	0.0287	47.75
5.	Bi_2Se_3/Bi_2WO_6	0.0281	0.0320	53.24
6.	Bi_2Se_3/N-Bi_2WO_6	0.0204	0.0397	66.06

4.3.2.6. Morphological Investigations of the wear scar surface

Surface scrutinizing techniques like SEM and AFM were availed to examine the morpho logy of the worn path on the steel ball tested with blends of additives following the ASTM D4172 norms. The SEM images of the wear scar pathway lubricated with plain PO and its admixtures with different additives (0.050% w/v) are exhibited in Figure 4.9. For the base lube, the extremely ridged surface due to frightful scratches can be viewed from the SEM micrograph. However, the smoothness of the worn surface is immensely enhanced by adding additives. The extent of surface upgradation validates the order of studied

tribological characteristics of the admixtures. The MWD measurements furnished in the inset of the portraits agree reasonably well with the evenness of the surface. The remarkable cutback in MWD are; plain oil (0.735 mm), Bi_2Se_3 (0.600 mm), Bi_2WO_6 (0.570 mm), N-Bi_2WO_6 (0.530 mm), Bi_2Se_3/Bi_2WO_6 (0.470 mm) and Bi_2Se_3/N-Bi_2WO_6 (0.430 mm). A splendid smooth surface is, thus, obtained when the oil with doped hybrid is employed for lubrication.

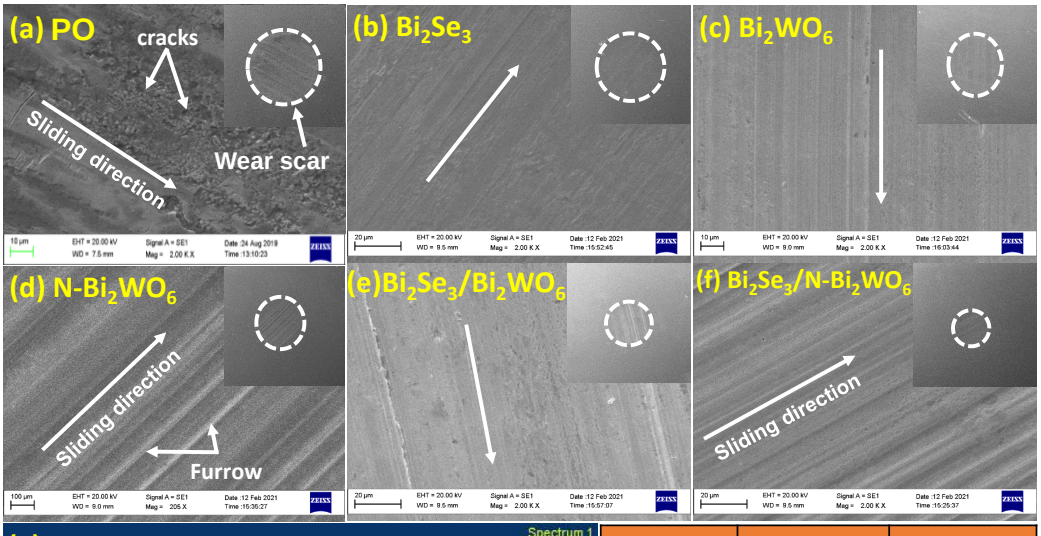

Element	Weight%	Atomic%
N K	0.60	2.10
O K	4.86	15.03
Fe K	92.52	81.95
Se L	1.06	0.66
W M	0.54	0.15
Bi M	0.43	0.10
Totals	100.00	

Figure 4.9. (a)-(f) SEM micrographs of the depleted surfaces lubricated with plain PO and blended additives (0.05% w/v) at 2.00 KX magnification following the ASTM D4172 norms, inset discerning wear scar surface at a higher magnification of 100 KX (g) EDX spectrum of wear track lubricated with Bi_2Se_3/N-Bi_2WO_6

EDX elucidation of worn surfaces lubricated with doped hybrid Bi_2Se_3/N-Bi_2WO_6 (Figure 4.9g) and other additives (Figure 4.10) identified all the constituent elements Bi, Se, N, W, and O, which is indicative of their successful adsorption on the wear track.

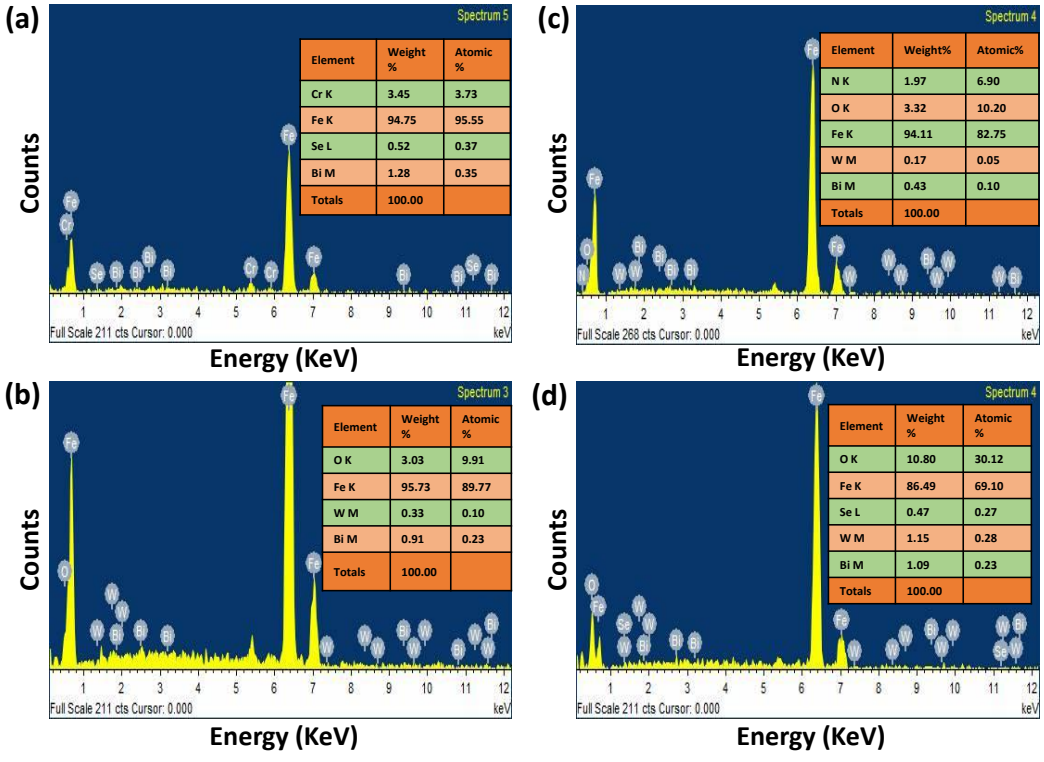

Figure 4.10. EDX spectrum of wear track of steel surface lubricated with (a) Bi_2Se_3, (b) Bi_2WO_6, (c) N-Bi_2WO_6 and (d) Bi_2Se_3/Bi_2WO_6

Moreover, contact-mode AFM was utilized to analyze the surface roughness of lubricated steel balls with the presence and absence of additives tested under the ASTM D4172 test. Figure 4.11 delineates the two and three-dimensional AFM photographs of the worn scar surfaces. The details of the surface roughness values for different admixtures, Sq and Rq area roughness and line roughness, respectively, are furnished in Figure 4.11. A massive reduction in the Rq (919 nm to 98 nm) and Sq (626 nm to 94 nm) values was noted from

plain base lube to doped nanohybrid. As anticipated, maximum smooth surface and minimum roughness are apparent from the Figure when the doped nanohybrid is utilized as an additive. Therefore, AFM findings supported fairly well the results of the SEM analysis. Furthermore, additional roughness parameters such as Ra, Rm, Rq, Rp, Ry, Rv, Sa, Sm, Sp, Sq, Sy, and Sv also substantiated the tribological results and are given in Table 4.2.

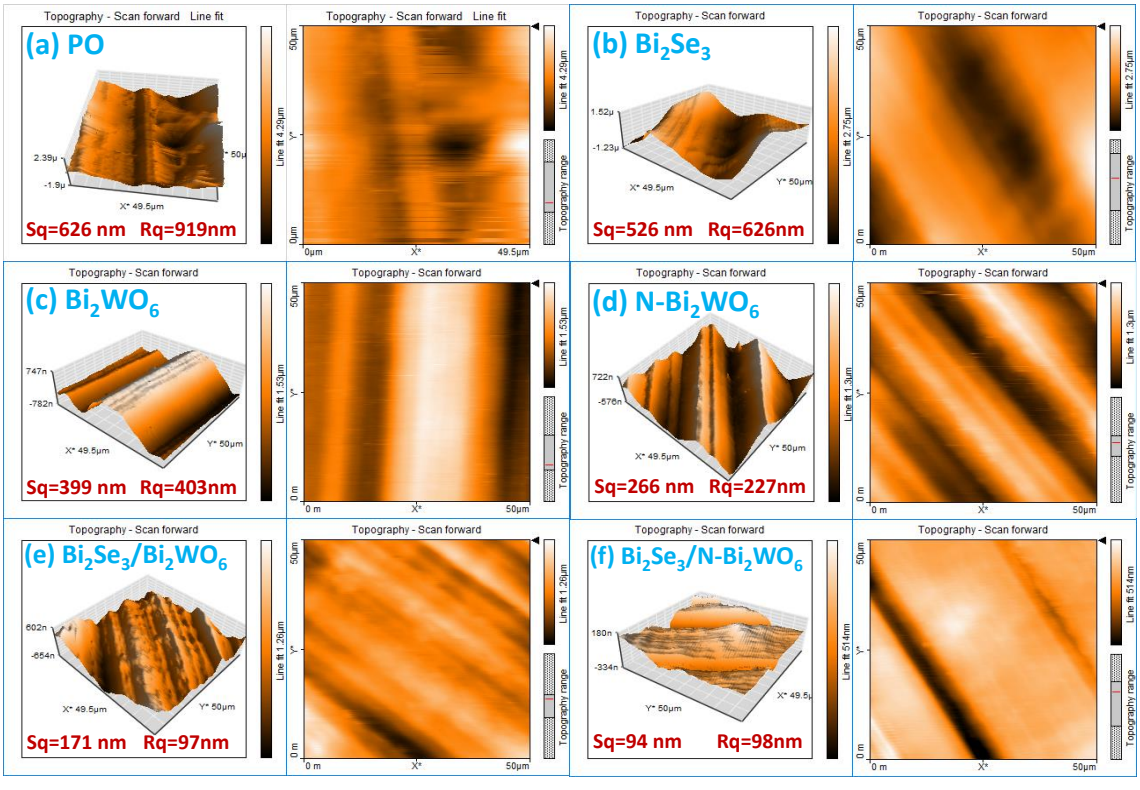

Figure 4.11. 3D and 2D AFM images of the wear track lubricated with PO and its admixtures (0.05% w/v) after ASTM D4172 test, (a) PO, (b) Bi_2Se_3, (c) Bi_2WO_6, (d) N-Bi_2WO_6, (e) Bi_2Se_3/Bi_2WO_6 and (f) Bi_2Se_3/N-Bi_2WO_6

Table 4.2. Surface roughness parameters obtained from the digital processing software of AFM (Nanosurf-basic Scan-2) for different additives after the antiwear test

Surface roughness parameter	**Sq (nm)**	**Rq (nm)**	**Sa (nm)**	**Ra (nm)**	**Sy (nm)**	**Ry (nm)**	**Sp (nm)**	**Rp (nm)**	**Sv (nm)**	**Rv (nm)**	**Sm (pm)**	**Rm (pm)**
PO	626	919	488	771	4363	3255	2611	2060	-1752	-1195	129	-129
Bi_2Se_3	526	626	443	538	2653	2232	1489	1244	-1164	-987	153	144
Bi_2WO_6	399	403	345	347	1469	1310	726	648	-742	-662	93	57
N- Bi_2WO_6	266	227	225	191	1226	820	672	374	-553	-445	185	217
Bi_2Se_3/ Bi_2WO_6	171	97	130	76	1163	498	568	160	-594	-338	127	218`
Bi_2Se_3/N- Bi_2WO_6	94	98	66	74	566	399	173	124	-392	-275	136	140

Where, S = Areal roughness, and R = Linear roughness parameters.

Sq = root mean square height, Rq = root mean square line

Sa = Arithmetical mean height, Ra = Arithmetic mean line

Sy = Maximum height of the surface, Ry = Maximum height of the profile

Sp = Maximum peak height, Rp = Maximum profile peak height

Sv = Maximum valley depth, Rv = Maximum profile valley depth

Sm = Mean width area, Rm = Mean width line

4.3.2.7. XPS Analysis of Tribofilm

The XPS spectra of the wear scar smeared with the doped hybrid were recorded after the ASTM D4172 antiwear test to specify the chemical states of the elemental components in the tribofilm developed *in situ.* The deconvoluted core level spectra of Bi 4f, Se 3d, N 1s, O 1s, W 4f, and Fe 2p are depicted in Figure 4.12a-f using peak fit software. The XP spectrum of Bi 4f is shown in Figure 4.12a, where Bi $4f_{7/2}$ and $4f_{5/2}$ can be assigned at

binding energies of 158.3 and 163.6 eV, respectively, for the Bi-O bond, while 157.5, 162.9 eV, respectively for the Bi-Se bond. The Bi-O bond is most likely formed due to the oxidation of Bi_2Se_3 under test conditions.[50,51] The existence of an additional peak at 58.1 eV in the Se 3d spectrum (Figure 4.12b) corresponds to SeO_2, showing the oxidation of Bi_2Se_3.[51,52] The peak positioning in the spectra of N 1s and O 1s is pretty much similar to the XP spectrum of the doped hybrid before the test (Figures 4.12c and 4.12d). The peak position in the W 4f spectrum (Figure 4.12e) is ascribed to the W-N, and the W-O bonds, indicating the formation of tungsten nitride and WO_3 during the tribochemical process.[53,54]

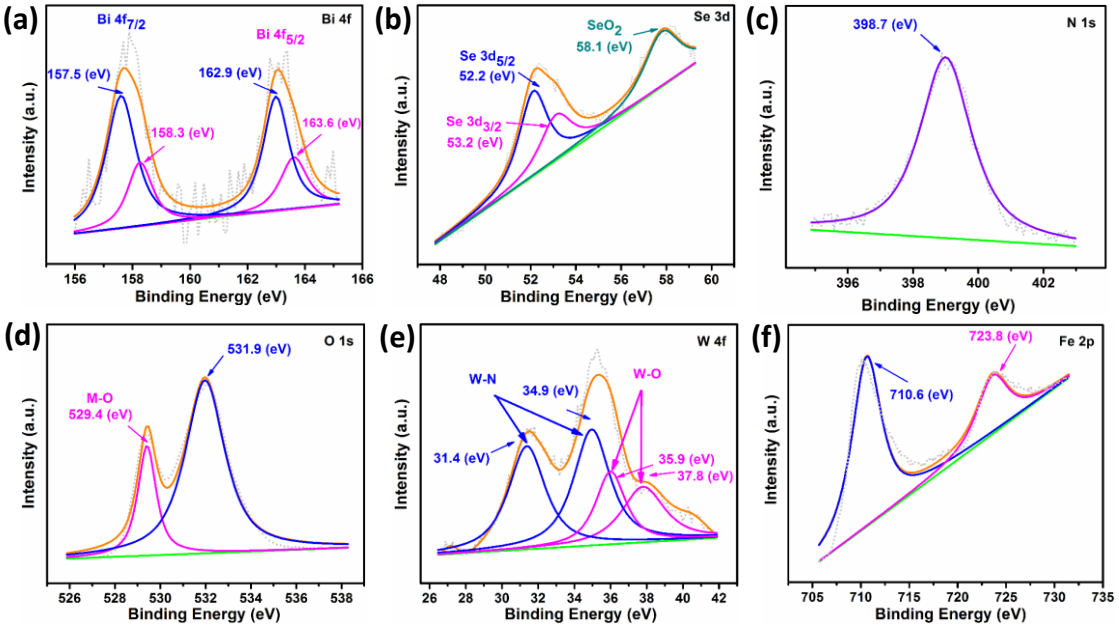

Figure 4.12. Deconvoluted XPS of the tribofilm generated on the wear track in the presence of PO blended with Bi_2Se_3/N-Bi_2WO_6 after ASTM D4172 test (a) Bi 4f (b) Se 3d (c) N 1s (d) O 1s (e) W 4f and (f) Fe 2p

The XPS studies indicate the formation of bismuth, selenium, and tungsten oxides due to tribochemical oxidation. Besides this, evidence was also found for tungsten nitride, which possesses lubricating behavior.[55,56] Further, the peaks that appeared in the XP spectrum of Fe 2p at 710.6 eV and 723.8 eV for Fe $2p_{3/2}$ and Fe $2p_{1/2}$ suggest the oxidation of Fe of the steel ball surface to Fe_2O_3 (Figure 4.12f).[57-62] Thus, according to the identification of tribofilm by XPS spectra, it can be inferred that tribofilm consists of tribochemically oxidized metal oxides (Bi_2O_3, SeO_2, WO_3, Fe_2O_3, etc.) and tungsten nitride which have synergized substantially to enhance the tribological activity.

4.3.2.8. Tentative lubrication mechanism

Quintessential two-dimensional layered materials, in general, have very low interlaminar shear strength because of weak van der Waals between adjacent layers.[63,64] The lubricating film formed by them keeps the two contact surfaces quite apart during the sliding process, thus reducing friction and wear significantly.[2,3] Accordingly, the nano lamellar bismuth selenide and bismuth tungstate individually have substantially reduced friction and wear. When put together in the hybrid bismuth selenide/bismuth tungstate, both nanosheets have prevented their agglomeration and furthered their layered morphology during lubrication rather than shattering into tiny particles.[2,3,65] Due to outstanding dispersibility in base lube, the hybrid can readily access the interface of the tribo-pairs.[66] The hetero lamellar structure in the hybrid provides random van der Waals heterojunctions associated with incongruous lattice debilitating further the interlaminar shear strength and, above all, the restacking tendencies.[63-66] Consequent to the alleviation of restacking, friction and wear are vehemently curtailed to the extent that the coefficient

of friction is reduced significantly.[2,3,63-66] For a thorough comprehension of the lubrication mechanism, the schematic illustration is provided in Figure 4.13.

XPS of the tribofilm generated on the wear track in the presence of PO blended with Bi_2Se_3/N-Bi_2WO_6 after the ASTM D4172 test discerns the presence of metal oxides as a result of tribochemical oxidation (Bi_2O_3, SeO_2, WO_3, Fe_2O_3, etc.), and tungsten nitride which have synergized altogether leading to effective enhancement in the tribological efficiency.

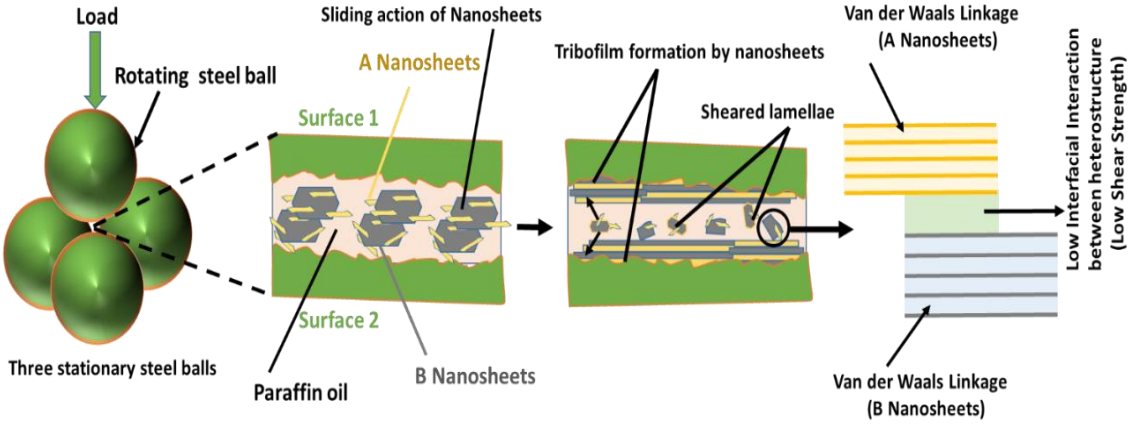

Figure 4.13. The diagrammatic representation of the proposed lubricating mechanism

4.4. Conclusions

The 2D- materials were chosen to design composites for extensive reduction of friction and wear because of their inherent characteristics specifically weak van der Waals forces between the proximal layers, providing lubricating properties along with high dispersibility. The preparation of bismuth selenide and bismuth tungstate nanosheets was achieved hydrothermally. Bismuth tungstate nanosheets were introduced onto bismuth selenide to increase the tribological activity. The layered morphology of bismuth selenide

and bismuth tungstate was instrumental in synergizing the activity of the composite. Hydrothermally synthesized nitrogen-doped bismuth tungstate was used to form the composite with bismuth selenide for further advancement of activity. Appraisal of tribological activity based on the ASTM D4172 and D5183 tests revealed the tremendous significance of layered morphology and nitrogen doping in the results. HR-SEM and TEM examinations of Bi_2Se_3/Bi_2WO_6 and Bi_2Se_3/N-Bi_2WO_6 composites discern Bi_2WO_6/N-Bi_2WO_6 nanosheets physically adorning Bi_2Se_3 nanosheets. FT-IR, p-XRD, and XPS studies were used to characterize the as-synthesized nanomaterials. UV/visible spectroscopy technique has been used to investigate the dispersion stability of the nanomaterial blends in PO. Even after 72 h, the most stable system was found to be Bi_2Se_3/N-Bi_2WO_6. As per the tests mentioned above, the tribological assessment of the blends at the optimal concentration (0.05 percent w/v) demonstrated the best efficiency of Bi_2Se_3/N-Bi_2WO_6 in reducing friction and wear. The next was Bi_2Se_3/Bi_2WO_6, followed by N-Bi_2WO_6, Bi_2WO_6, and Bi_2Se_3. SEM and AFM analyses of the wear track support the order of efficiency. According to the XPS study of the worn pathway of Bi_2Se_3/N-Bi_2WO_6, the tribofilm contains oxides of Bi, Se, W, and Fe_2O_3 and tungsten nitride leading to enhancement in the tribological efficiency. Doping nitrogen into bismuth tungstate led to the formation of defects, which improved lubricating characteristics. Undoubtedly, the phenomenal tribological activity of Bi_2Se_3/N-Bi_2WO_6 could be attributed to the hetero lamellar structure, which assisted in preventing restacking and nitrogen doping.

4.5. References

(1) Zhang, W.; Cao, Y.; Tian, P.; Guo, F.; Tian. Y.; Zheng, W.; Ji, X.; Liu, J. Soluble, exfoliated two-dimensional nanosheets as excellent aqueous lubricants. *ACS Appl. Mater. Interfaces* **2016**, *8(47)*, 32440-32449.

(2) Shukla, N.; Verma, D. K.; Singh, A. K.; Kumar, B.; Kavita; Rastogi, R. B. Ternary composite of methionine-functionalized graphene oxide, lanthanum-doped yttria nanoparticles, and molybdenum disulfide nanosheets for thin-film lubrication. *ACS Appl. Nano Mater*. **2020**, *3(8)*, 8012-8026.

(3) Verma, D. K.; Shukla, N.; Kumar, B.; Singh, A.K.; Shahu, K.; Yadav, M.; Rhee, K. Y.; Rastogi, R. B. Synergistic tribo-activity of nanohybrids of zirconia/cerium-doped zirconia nanoparticles with nano lamellar reduced graphene oxide and molybdenum disulfide. *Nanomaterials* **2020**, *10(4)*, 707.

(4) Rajendhran, N.; Palanisamy, S.; Periyasamy, P.; Venkatachalam, R. Enhancing of the tribological characteristics of the lubricant oils using Ni-promoted MoS_2 nanosheets as nano-additives. *Tribol. Int*. **2018**, *118*, 314-328.

(5) Yi, M.; Qiu, J.; Xu, W. Tribological performance of ultrathin MoS_2 nanosheets in formulated engine oil and possible friction mechanism at elevated temperatures. *Tribol. Int*. **2022**, *167*, 107426.

(6) Jia, X.; Huang, J.; Li, Y.; Yang, J.; Song, H. Monodisperse Cu nanoparticles@ MoS_2 nanosheets as a lubricant additive for improved tribological properties. *Appl. Surf. Sci*. **2019**, *494*, 430-439.

(7) Zhang, X.; Xu, H.; Wang, J.; Ye, X.; Lei, W.; Xue, M.; Tang, H.; Li, C. Synthesis of ultrathin WS_2 nanosheets and their tribological properties as lubricant additives. *Nanoscale Res. Lett*. **2016**, *11(1)*, 1-9.

(8) Zhang, X.; Wang, J.; Xu, H.; Tan, H.; Ye, X. Preparation and tribological properties of WS_2 hexagonal nanoplates and nanoflowers. *Nanomaterials* **2019**, *9(6)*, 840.

(9) Zhu, J.; Zeng, Q.; Yan, C.; He, W. WS_2 nanopowders as high-temperature lubricants: an experimental and theoretical study. *ACS Appl. Nano Mater*. **2019**, *2(9)*, 5604-5613.

(10) Ouyang, T.; Lei, W.; Tang, W.; Shen, Y.; Mo, C. Experimental investigation of the effect of IF-WS_2 as an additive in castor oil on tribological property. *Wear* **2021**, *486*, 204070.

(11) Chen, J.; Yang, J.; Chen, B.; Liu, S.; Dong, J.; Li, C. Large-scale synthesis of $NbSe_2$ nanosheets and their use as nanofillers for improving the tribological properties of epoxy coatings. *Surf. Coat. Technol.* **2016**, *305*, 23-28.

(12) Changsheng, L.; Maode, H.; Yanqing, L.; Yun, Y. Synthesized and tribological researching of $NbSe_2$ fibers. *3rd IEEE International Conference on Nano/Micro Engineered and Molecular Systems* **2008**, 337-341.

(13) Yang, J.; Yao, H.; Liu, Y.; Zhang, Y. Synthesis and tribological properties of WSe_2 nanorods. *Nanoscale Res. Lett.* **2008**, *3(12)*, 481-485.

(14) Cao, K.; Li, C.; Yonghua, C.; Tang, H.; Yan, F.; Song, H.; Yang, X. Graphite-controlled fabrication of ultrathin WSe_2 nanosheets with tower-like structure and their tribological properties. *Tribol. Trans*. **2012**, *55*(3), 297-301.

(15) Li, W.; Hu, L.; Wang, M.; Tang, H.; Li, C.; Liang, J.; Jin, Y.; Li, D. Synthesis and tribological properties of Mo-doped WSe_2 nanolamellars. *Cryst. Res. Technol*. **2012**, *47(8)*, 876-881.

(16) Zhang, X.; Tang, H.; Lla, CH.; Chen, S. Synthesis and tribological properties of Nb-doped $MoSe_2$ nanoplates. *Chalcogenide Lett*. **2013**, *10(10)*, 403-409.

(17) Li, J. F.; Chen, B.; Shi, Q.; CHU, Y.; LI, C. Tribological properties of novel Cu/$NbSe_2$ composites reinforced with reduced graphene oxide filler. *Chalcogenide Lett.* **2017**, *14(11).*

(18) Ambrosi, A.; Sofer, Z.; Luxa, J.; Pumera, M. Exfoliation of layered topological insulators Bi_2Se_3 and Bi_2Te_3 via electrochemistry. *ACS Nano*. **2016**, *10(12)*, 11442-11448.

(19) Müller, C.; Redondo, F. L.; Dennehy, M.; Ciolino, A. E.; Tuckart, W. R. Bismuth (III) sulfide as additive: towards better lubricity without toxicity. *Ind. Lubr. Tribol*. **2018**, *70(2)*, 347-352.

(20) Hart, R. T.; Kerr, A. A.; Eckert, N. A. Bismuth sulfide (Bi_2S_3) as the active species in extreme pressure lubricants containing bismuth carboxylates and sulfur compounds. *Tribol. Trans*. **2009**, *53(1)*, 22-28.

(21) Gonzalez-Rodriguez, P.; van den Nieuwenhuijzen, K. J.; Lette, W.; Schipper, D. J.; Ten Elshof, J. E. Tribochemistry of bismuth and bismuth salts for solid lubrication. *ACS Appl. Mater. Interfaces* **2016**, *8(11)*, 7601-7606.

(22) Pilotti, B.; Prieto, G.; Juan, A.; Faccio, R.; Broitman, E.; Dennehy, M.; Tuckart, W. R. Bi_2S_3 and MoS_2 soft coatings: a comparative study of their frictional behavior under different humidity levels, normal loads, and sliding speeds. *Tribol. Lett.* **2021**, *69(3)*, 1-24.

(23) Wang, J.; Tang, A.; Tan, L.; Yang, H.; Ouyang, J. Morphological evolution of hierarchical Bi_2Se_3/BiOBr nanostructures and enhanced activity for p-nitrophenol reduction by $NaBH_4$. *Cryst. Eng. Comm.* **2017**, *19(32)*, 4824-4831.

(24) Li, X. B.; Li, Y. F. Tribological Properties of Spark Plasma Sintering TZ3Y20A–$SrMoO_4$ Composites at Elevated Temperature. *Tribol. Lett*. **2017**, *65(4)*, 1-10.

(25) Zhu, S.; Bi, Q.; Kong, L.; Yang, J. U.; Liu, W. Barium chromate as a solid lubricant for nickel aluminum. *Tribol. Trans.* **2012**, *55(2)*, 218-223.

(26) Li, Y. F.; Yin, H.; Li, X. L.; Mao, C. C. Friction and Wear Properties of Spark Plasma Sintering NiCr–$SrSO_4$ Composites at Elevated Temperatures in Sliding Against Alumina Ball. *Tribol. Lett.* **2016**, *64(2)*, 1-10.

(27) Kostornov, A. G.; Pasichnyi, V. V.; Fushchich, O. I.; Varchenko, V. T.; Korchemnaya, V. S. Copper tungstate produced from tungsten-containing waste as addition to antifriction material. *Powder Metall. Met. Ceram.* **2009**, *48(11)*, 718-722.

(28) Zhu, S.; Bi, Q.; Yang, J.; Liu, W. Tribological property of Ni_3Al matrix composites with addition of $BaMoO_4$. *Tribol. Lett.* **2011**, *43(1)*, 55-63.

(29) Liu, E.; Bai, Y.; Gao, Y.; Yi, G.; Jia, J. Tribological properties of NiAl-based composites containing Ag_3VO_4 nanoparticles at elevated temperatures. *Tribol. Int.* **2014**, *80*, 25-33.

(30) Zhu, S.; Bi, Q.; Yang, J.; Liu, W. Ni_3Al matrix composite with lubricious tungstate at high temperatures. *Tribol. Lett*. **2012**, *45(2)*, 251-255.

(31) Hu, S.; Wang, B.; Ma, Y.; Li, M.; Zhang, L.; Huang, Z. Ultrathin bismuth tungstate nanosheets as an effective photo-assisted support for electrocatalytic methanol oxidation. *J. Colloid Interface Sci*. **2019**, *552*, 179-185.

(32) Liu, Z.; Liu, X.; Wei, L.; Yu, C.; Yi, J.; Ji, H. Regulate the crystal and optoelectronic properties of Bi_2WO_6 nanosheet crystals by Sm^{3+} doping for superior visible-light-driven photocatalytic performance. *Appl. Surf. Sci*. **2020**, *508*, 145309.

(33) Dumrongrojthanath, P.; Thongtem, T.; Phuruangrat, A.; Thongtem, S. Synthesis and characterization of hierarchical multilayered flower-like assemblies of Ag doped Bi_2WO_6 and their photocatalytic activities. *Superlattices Microstruct*. **2013**, *64*, 196-203.

(34) Singh, A. K.; Shukla, N.; Verma, D. K.; Kavita.; Kumar, B.; Rastogi, R.B. Enhancement of Triboactivity of Nanolamellar Graphitic-C_3N_4 by N-Doped ZnO Nanorods. *Ind. Eng. Chem. Res*. **2021**, *60(2)*, 864-874.

(35) Singh, A. K.; Shukla, N.; Verma, D. K.; Kumar, B.; Mandal, K. D.; Rastogi, R.B. Reinforcement of nanoporous lanthanum-doped zinc borate by vanadium selenide nanosheets for improved tribological activity. *RSC Adv.* **2022**, *12(29)*, 18685-18696.

(36) Verma, D. K.; Kumar, B.; Kavita.; Rastogi, R. B. Zinc oxide-and magnesium-doped zinc oxide-decorated nanocomposites of reduced graphene oxide as friction and wear modifiers. *ACS Appl. Mater. Interfaces* **2018**, *11(2)*, 2418-2430.

(37) Hou, K.; Wang, J.; Yang, Z.; Ma, L.; Wang, Z.; Yang, S. One-pot synthesis of reduced graphene oxide/molybdenum disulfide heterostructures with intrinsic incommensurateness for enhanced lubricating properties. *Carbon* **2017**, *115*, 83-94.

(38) Leven, I.; Krepel, D.; Shemesh, O.; Hod, O. Robust superlubricity in graphene/h-BN heterojunctions. *J. Phys. Chem. Lett.* **2013**, *4(1)*, 115-120.

(39) Xu, Z. D.; Xin, J. B.; Fan, R. X.; Wang, K.; Yang, J. A simple approach to fabricate gC $_3N_4$/MoS_2 nanocomposite and its application as a lubricant additive. *Dig. J. Nanomater. Biostruct.* **2018**, *13(3)*, 731-741.

(40) Tang, B.; Jiang, G.; Wei, Z.; Li, X.; Wang, X.; Jiang, T.; Chen, W.; Wan, J. Preparation of N-doped Bi_2WO_6 microspheres for efficient visible light-induced photocatalysis. *Acta. Metall. Sin. Engl. Lett.* **2014**, *27(1)*, 124-130.

(41) Xu, H.; Chen, G.; Jin, R.; Chen, D.; Wang, Y.; Pei, J.; Zhang, Y.; Yan, C.; Qiu, Z. Microwave-assisted synthesis of Bi_2Se_3 ultrathin nanosheets and its electrical conductivities. Cryst. Eng. Comm. **2014**, *16(19)*, 3965-3970.

(42) Zang, C.; Qi, X.; Ren, L.; Hao, G.; Liu, Y.; Li, J.; Zhong, J. Photoresponse properties of ultrathin Bi_2Se_3 nanosheets synthesized by hydrothermal intercalation and exfoliation route. *Appl. Surf. Sci.* **2014**, *316*, 341-347.

(43) Zhou, F.; Zhao, Y.; Zhou, W.; Tang, D. Temperature-dependent Raman scattering of large size hexagonal Bi_2Se_3 single-crystal nanoplates. *Appl. Sci*. **2018**, *8(10)*, 1794.

(44) El-Fattah, A.; Ashoush, M. A. Structural characterization of pure and magnetic-doped Bi_2Se_3 nanoparticles. *J. Mater. Sci.: Mater. Electron*. **2018**, *29(3)*, 2593-2599.

(45) Li, H.; Li, N.; Wang, M.; Zhao, B.; Long, F. Synthesis of novel and stable g-C_3N_4-Bi_2WO_6 hybrid nanocomposites and their enhanced photocatalytic activity under visible light irradiation. *Royal Soc. Open Sci*. **2018**, *5(3)*, 171419.

(46) Chen, D.; Wen, H.; Li, T.; Yin, L.; Fan, B.; Wang, H.; Zhang, R.; Li, X.; Xu, H.; Lu, H.; Yang, D. Novel pseudo-morphotactic synthesis and characterization of tungsten nitride nanoplates. *J. Solid State Chem.* **2011**, *184(2)*, 455-462.

(47) Huang, Y.; Wang, K.; Guo, T.; Li, J.; Wu, X.; Zhang, G. Construction of 2D/2D Bi_2Se_3/g-C_3N_4 nanocomposite with high interfacial charge separation and photo-heat conversion efficiency for selective photocatalytic CO_2 reduction. *Appl. Catal. B: Environ.* **2020**, *277*, 119232.

(48) Huang, J.; Li, X.; Su, G.; Gao, R.; Wang, W.; Dong, B.; Cao, L. Construction of layer-by-layer g-C_3N_4/Ag/Bi_2WO_6 Z-scheme system with enhanced photocatalytic activity. *J. Mater. Sci.* **2018**, *53(23)*, 16010-16021.

(49) Hoang, L. H.; Phu, N. D.; Peng, H.; Chen, X. B. High photocatalytic activity N-doped Bi_2WO_6 nanoparticles using a two-step microwave-assisted and hydrothermal synthesis. *J. Alloys Compd*. **2018**, *744*, 228-233.

(50) Meng, A.; Yuan, X.; Shen, T.; Li, Z.; Jiang, Q.; Xue, H.; Lin, Y.; Zhao, J. One-step synthesis of flower-like Bi_2O_3/Bi_2Se_3 nanoarchitectures and $NiCoSe_2/Ni_{0.85}Se$ nanoparticles with appealing rate capability for the construction of high-energy and long-cycle-life asymmetric aqueous batteries. *J. Mater. Chem. A* **2019**, *7(29)*, 17613-17625.

(51) Yang, T.; Liu, J.; Yang, D.; Mao, Q.; Zhong, J.; Yuan, Y.; Li, X.; Zheng, X.; Ji, Z.; Liu, H.; Wang, G. Bi_2Se_3@C rod-like architecture with outstanding electrochemical properties in lithium/potassium-ion batteries. *ACS Appl. Energy Mater*. **2020**, *3(11)*, 11073-11081.

(52) Hobbs, R. G.; Schmidt, M.; Bolger, C. T.; Georgiev, Y. M.; Fleming, P.; Morris, M. A.; Petkov, N.; Holmes, J. D.; Xiu, F.; Wang, K. L.; Djara, V. Resist–substrate interface tailoring for generating high-density arrays of Ge and Bi_2Se_3 nanowires by electron beam lithography. *J. Vac. Sci. & Technol. B Nanotechnol. Microelectron*. **2012**, *30(4)*, 041602.

(53) Zhu, Y.; Chen, G.; Zhong, Y.; Zhou, W.; Shao, Z. Rationally Designed Hierarchically Structured Tungsten Nitride and Nitrogen-Rich Graphene-Like Carbon Nanocomposite as Efficient Hydrogen Evolution Electrocatalyst. *Adv. Sci.* **2018**, *5(2)*, 1700603.

(54) Chen, Q.; Li, X.; Xie, R.; Xu, L.; Liu, L. Novel rapid synthesis of nanoscale tungsten nitride using non-toxic nitrogen source. *Ceram. Int.* **2020**, *46(2)*, 2580-2584.

(55) Ju, H.; Ding, N.; Xu, J.; Yu, L.; Asempah, I.; Xu, J.; Yi, G.; Ma, B. Crystal structure and the improvement of the mechanical and tribological properties of tungsten nitride films by addition of titanium. *Surf. Coat. Technol.* **2018**, *345*, 132-139.

(56) Tsai, Y. Z.; Duh, J. G. Tribological behavior of CrN/WN multilayer coatings grown by ion-beam assisted deposition. *Surf. Coat. Technol.* **2006**, *201(7)*, 4266-4272.

(57) Singh, A. K.; Yadav, A.; Indra, A.; Rastogi, R. B. Superior performance of ultrathin metal organic framework nanosheets for antiwear and antifriction testing. *Colloids Surf. A Physicochem. Eng. Asp.* **2021**, *613*, 126100.

(58) Singh, A. K.; Shukla, N.; Verma, D. K.; Kumar, B.; Singh, S.; Rastogi, R. B. Polyaniline intercalated vanadium pentoxide nanosheets for the improvement of lubricity of base oil. *Colloids Surf. A Physicochem. Eng. Asp.* **2022**, *642*, 128644.

(59) Kumar, B.; Verma, D. K.; Shukla, N.; Singh, A. K.; Rastogi, R. B. Ionic liquid stabilized Ag@ C composite for improvement of triboactivity. *J. Mol. Liq*. **2020**, *307*, 113012-113021.

(60) Kumar, B.; Verma, D. K.; Singh, A. K.; Kavita.; Shukla, N.; Rastogi, R. B. Nanohybrid Cu@ C: synthesis, characterization and application in enhancement of lubricity. *Compos. Interfaces* **2019**, 777-794.

(61) Verma, D. K.; Kuntail, J.; Kumar, B.; Singh, A. K.; Shukla, N.; Kavita.; Sinha, I.; Rastogi, R. B. Amino Borate-Functionalized Reduced Graphene Oxide Further Functionalized with Copper Phthalocyanine Nanotubes for Reducing Friction and Wear. *ACS Appl. Nano Mater.* **2020**, *3*, 5530-5541.

(62) Singh, A. K.; Shukla, N.; Kumar, B.; Verma, D. K.; Maurya, J. L.; Singh, S.; Rastogi, R. B. Improvement of tribo-active behavior of g-C_3N_4 nanosheets using m-$LaVO_4$ nanoparticles. *Colloids Surf. A Physicochem. Eng. Asp.* **2023**, *663*, 131031.

(63) Chouhan, A.; Sarkar, T. K.; Kumari, S.; Vemuluri, S.; Khatri, O. P. Synergistic lubrication performance by incommensurately stacked ZnO-decorated reduced graphene oxide/MoS_2 heterostructure. *J. Colloid Interface Sci*. **2020**, *580*, 730-739.

(64) Kumari, S.; Chouhan, A.; Konathala, L. S. K.; Sharma, O. P.; Ray, S. S.; Ray, A.; Khatri, O. P. Chemically functionalized 2D/2D hexagonal boron Nitride/Molybdenum disulfide heterostructure for enhancement of lubrication properties. *Appl. Surf. Sci*. **2022**, *579*, 152157.

(65) Zhou, S.; Wang, F.; Chen, J.; Alhashmialameer, D.; Wang, S.; Mahmoud, M. H. H.; Mersal, G. A.; Huang, J.; Zhang, Q.; Zhao, G.; Liu, Y. Enhanced mechanical, thermal, and tribological performance of 2D-laminated molybdenum disulfide/RGO

nanohybrid filling phenolic resin composites. *Adv. Compos. Hybrid Mater*. **2022**, *5(2)*, 1206-1220.

(66) Guo, P.; Qi, S.; Chen, L.; Gou, C.; Lin, B.; Lu, Z.; Wu, Z.; Zhang, G. Black phosphorus–graphene oxide hybrid nanomaterials toward advanced lubricating properties under water. *Adv Mater. Interfaces* **2019**, *6(23)*, 1901174.